Journal of Materials Chemistry A

Intercalation of Ferrocene into Vanadyl Phosphate by Density Functional Theory.

Journal:	*Journal of Materials Chemistry A*
Manuscript ID	TA-ART-11-2023-007097.R2
Article Type:	Paper
Date Submitted by the Author:	30-Apr-2024
Complete List of Authors:	Liu, Yuan; University of Florida, Ta, An; University of Florida Ullberg, Seaton; University of Florida Liu, Jiahui; University of Florida Talham, Daniel R.; University of Florida Simon, Phillpot; University of Florida

Intercalation of Ferrocene into Vanadyl Phosphate by Density Functional Theory

Yuan Liu (刘源)[1], An T. Ta[1], R. Seaton Ullberg[1], Jiahui Liu[2], Daniel R. Talham[2] and Simon R. Phillpot[1*]

[1]Department of Materials Science and Engineering, University of Florida, Gainesville FL 32611 USA

[2]Department of Chemistry, University of Florida, Gainesville FL 32611 USA

To be submitted to Journal of Materials Chemistry A

Abstract

Vanadyl phosphate ($VOPO_4$) is often studied as an intercalation host with both atomic and molecular guests as battery electrodes and for related energy storage applications. Among redox active guests, metallocene, primarily ferrocene, are frequently employed. Here, a systematic investigation of 17 possible configurations of the intercalation of ferrocene into $VOPO_4$, revealed the existence of 14 structurally distinct configurations. Among these configurations, the most stable was determined to be that of ferrocene intercalated between a vanadium and oxygen-vanadium site, with the carbon-hydrogen apex from the cyclopentadienyl rings facing the vanadium atom, and the axis of ferrocene rotated by 45° with respect to the [100] direction of the (001) plane of the $VOPO_4$. Analysis of charge density distributions indicated a charge transfer between iron and vanadium, supporting the preference for ferrocene to intercalate between vanadium and oxygen-vanadium site rather than on a phosphorus site. When intercalated on the vanadium site, the cyclopentadienyl ring adopts an eclipsed arrangement, while it exhibited a gauche arrangement when intercalated on a phosphorus. Additionally, when the apical hydrogen was oriented towards the vanadium atom, there was a noticeable bend in the ferrocene. This bend can be attributed to both van der Waals interactions and the polarizable ion interaction between the ferrocene and the $VOPO_4$ layer, which supported by the electron localized function and the Hirshfeld surface analysis, respectively. Results provide new atomic level insights into how metallocene guest molecules interact with the layered $VOPO_4$ host.

Key words: vanadyl phosphate, ferrocene, density functional theory, intercalation

* Corresponding author: sphil@mse.ufl.edu

ORCIDS: YL: 0000-0003-3973-4207; AT: 0000-0002-2767-8343; RSU: 0000-0001-5138-1833; JL: 0009-0008-9444-7175; DRT: 0000-0003-1783-5285; SRP: 0000-0002-7774-6535

1. Introduction.

Vanadyl phosphate ($VOPO_4$) has garnered considerable attention as an intriguing material, owing to its potential applications in energy storage,[1,2,3,4] catalysis,[5,6,7,8,9] and ion conduction.[10] Due to the relatively weak interlayer bonds, neighboring layers of $VOPO_4$ exhibit relative independence, enabling ionic and molecular intercalation into the interlayer spaces. Several studies have focused on the intercalation of $VOPO_4$ with lithium,[11,12] sodium,[13] potassium[14], and zinc ions,[15] envisaging this complex material as a potential cathode in batteries. For example, recently, Zhu *et al.*[16] successfully intercalated zinc ions into $VOPO_4$, resulting in zinc-$VOPO_4$ composite cathodes.

Molecular intercalation into $VOPO_4$ is also of significant interest, having relevance to exfoliation processes, catalysis, and as an avenue for improving ion transport in $VOPO_4$ electrochemistry.[17,18] Molecular redox intercalations constitute a particularly interesting class of reactions as they allow for investigation of the redox intercalation host without the complications of incorporating the host into an electrode or interference with electrolytic processes.[19] For such studies, metallocene guests are attractive because of their reversible redox reactions; in addition, the metallocene sandwich structure means they form only weak specific interactions with inorganic surfaces and the galleries in which they intercalate, allowing focus on properties of the host. Recent studies of ferrocene intercalation into $VOPO_4$ highlight its utility.[20,21]

Recent experimental work has revealed how suspending solvents can change the surface energy, surface stress and associated internal effective pressure of layered colloidal solids leading to changes in solid-state phase behavior.[22] These same surface stress effects shown to influence physical phenomena can also affect chemical processes in solids when those processes are influenced by solid-state elastic properties, as recent DFT studies on the role of surface stresses on lithium-ion diffusion have explored. [23–25] We are, therefore, interested in ferrocene/$VOPO_4$ and related systems as platforms to better understand how changing host elastic properties correlate with guest diffusion and intercalation kinetics. While experimentally more accessible,[21,26–30] from

a theoretical standpoint molecular intercalation can be quite complex. Yes, density functional theory (DFT) is a powerful method for probing atomic level interactions making it a suitable approach to characterize intercalation products and diffusion pathways. This paper validates the approach by determining the most stable configurations of ferrocene located within the $VOPO_4$ layered galleries and revealing how a distortion from C_5 symmetry maximizes interaction with the $VOPO_4$ layers. The work provides valuable atomic level insights into molecular intercalation into these layered solid-state hosts and sets the groundwork for more complex questions about ion diffusion and the influence of changing host elastic properties on intercalation processes.

2. Computational Method and Structures.

2.1 Computational methods

The DFT calculations performed in this study utilized the Vienna Ab-initio Simulation Package (VASP) software,[31,32] employing the Perdew-Burke-Ernzerhof (PBE) exchange-correlation functional within the Generalized Gradient Approximation (GGA)[33] method. Projector-augmented wave (PAW)[34,35] pseudopotentials were utilized. For vanadium five valence electrons ($3d^4 4s^1$) were explicitly included, for phosphorus five ($3s^2 3p^3$), for iron eight ($3d^7 4s^1$), for oxygen six ($2s^2 2p^4$), and for carbon four ($2s^2 2p^2$). To ensure convergence of the calculations, a wave-function plane cut-off energy of 600 eV was employed. The DFT+U[36] method was adopted to account for electron localization in the 3d states of vanadium, with a U parameter for 3.25 eV.[37,38] The DFT+D3[39,40] correction was applied to better incorporate van der Waals interactions. To evaluate the solvent effect, we utilized the implicit solvation model facilitated by VASPsol.[41–43] For simulations conducted in a water environment, the default settings were utilized. Specifically, the bulk dielectric constant was set at 80, with all other parameters maintained at their default values.

The atomic structures were optimized using a conjugate gradient method[44,45] until the average force reached a value less than 0.025 eV/Å, with an energy tolerance of

1×10^{-6} eV for each electronic step. For the frequency calculations used in the estimates of the vibrational free energy, the energy tolerance is 1×10^{-7} eV. Spin-polarization was considered in all calculations. Gaussian smearing with a width of 0.05 eV was employed during optimizations.

In the case of pure vanadyl phosphate, a dense 8x8x12 gamma-centered point k-mesh was employed to obtain an accurate relaxed structure. However, when ferrocene was incorporated, to avoid interactions between neighboring ferrocene molecules due to periodic boundary conditions, we employed a 2x2x1 supercell of $VOPO_4$, see Figure 1a. Since incorporating the ferrocene into the vanadyl phosphonate layer leads to a large expansion in the c direction, this enabled us to use a k-mesh density of 4x4x5. The charge density difference calculations were performed using VASPKIT.[46] The visualization of structures were used CrystalMaker;[47] Electron localization function (ELF)[48] calculations were carried out with VESTA.[49] The Hirshfeld surface analysis[50] was implemented by the Mutlwfn 3.8,[51] and visualization by VMD.[52]

2.2 Vanadyl phosphate

Ferrocene intercalated vanadyl phosphate is readily synthesized starting with vanadyl phosphate dihydrate, $VOPO_4{\cdot}2H_2O$. The water molecules are lost in the ferrocene-intercalated product, so the host is better considered as dehydrated vanadyl phosphate, $VOPO_4$. The crystal structure of dehydrated vanadyl phosphate ($VOPO_4$) was sourced from the Material Project database, MP-19000.[53] In Figure 1a, the crystal structure unit cell is depicted and the corresponding structure parameters are provided in Table 1. The space group is P4/nmm, a tetragonal crystal structure characterized by a two-dimensional $VOPO_4$ sheet in the a-b plane, periodically repeated in the c direction, see Figure 1b. The phosphorus atoms are tetrahedrally coordinated to four oxygen atoms, with all P-O bond lengths measuring 1.54 Å. Two of the oxygens (colored blue in Figure 1) lie on the top surface of each $VOPO_4$ layer while the other two oxygens (colored red in Figure 1) lie on the bottom surface. The line between the two red atoms associated with a particular phosphorus is at 90˚ to the line joining the blue atoms; one

line lies in the [100] direction while the other lies in the [010] direction. Vanadium atoms form bonds with five oxygen atoms in a square pyramid configuration. Four V-O bonds form the non-flat base of the pyramid with equal length, 1.90 Å. Each of the oxygen in the base is associated with a different PO_4 tetrahedron; The V-O-P bond angle is approximately 131.91°. The fifth V-O bond defines the apex of the pyramid and lies in the c direction. The bond between the V and this apical oxygen is shorter, 1.60 Å, and is typical of vanadyl V-O bond lengths. This vanadyl apical oxygen is shown in pink in Figure 1 and subsequent figures. Half of the VO_5 pyramids point above the a-b plane and half below. Using the unit cell shown in Figure 1a, we see that rows of up-pointing and down-pointing VO_5 pyramids alternate along the b direction (y-axis); that is, they alternate in a checkerboard pattern in the [110] and [1-10] directions, See Figure 1c.

In Table 1, we show the dehydrated and hydrated forms of $VOPO_4$ from DFT results and compare with the experimental structures.[54] The a and b lattice parameters do not strongly change upon dehydration, and both DFT results agree very well with the experiment. We ascribe the slight difference between the a and b lattice parameters to the fact that the computational supercell for $VOPO_4{\cdot}2H_2O$ contains two $VOPO_4$ formula units and four waters; the a and b lattice parameters are thus sensitive to their specific arrangements. If we were to calculate a significantly larger unit cell, something which is computationally prohibitive, we would expect this difference to decrease significantly. The calculated c lattice parameter of the dehydrated system is much lower than that of the hydrated system. Upon hydration there is much better agreement between the calculation (7.273 Å) and the experiment (7.410 Å). The remaining ~2% difference arises from the weak secondary bonding between the layers. Indeed, a calculation of the energy of the system at the experimental lattice parameters yielded an energy of only 0.35 meV/atom higher than the structure shown in Table 1. This shows that the potential energy surface is very flat and, thus, there the c-lattice parameter cannot be determined with high precision.

Table 1. The lattice parameters of $VOPO_4$ by using GGA+U with D3 correction and compared with experimental data of $VOPO_4 \cdot 2H_2O$.

Lattice	$VOPO_4$ GGA+U_D3	$VOPO_4 \cdot 2H_2O$ GGA+U_D3	$VOPO_4 \cdot 2H_2O$ Experimental[54]
a (Å)	6.212	6.234	6.202
b (Å)	6.212	6.215	6.202
c (Å)	4.285	7.273	7.410
α °	90	90	90
β °	90	90	90
γ °	90	90	90

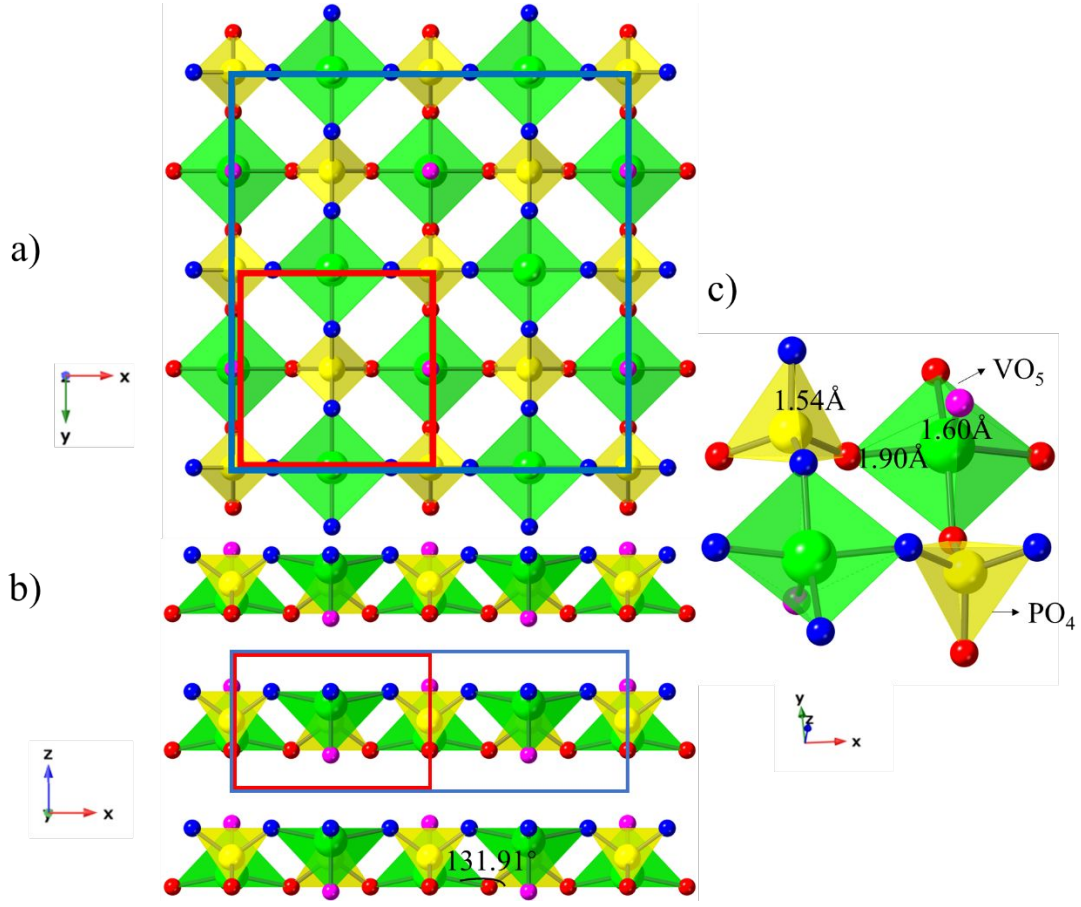

Figure 1. a) The crystal structure of dehydrated $VOPO_4$. Here and in subsequent figures, the vanadium is in green, phosphorus in yellow, the apical oxygen of the VO_5 pyramid

is pink, oxygen on the bottom of the layers (defined as -z) are red, and oxygen on top of the layers are blue. The red box is the unit cell, and the blue box is the 2*2*1 supercell; for clarity, we intentionally shift the red box to be slightly. b) The $VOPO_4$ sheets are periodically repeated in the c direction. c) The connection pattern between VO_5 and PO_4 polyhedral.

To confirm that this is the $VOPO_4$ structure's lowest total energy, we varied the in-plane position of one layer relative to the other in a calculation of a system with two layers. Based on the symmetry of vanadyl phosphate, we explored two types of displacement. Defining zero displacements as when the V atoms in one layer lie exactly over the top of the V atoms in the neighboring layer, we allowed two different layer sliding, one involved displacement along the [100] direction, as illustrated in Figure 2a, while the other entailed displacement along the [110] direction, depicted in Figure 2b. Figures 2c and 2d illustrate the total energy of the displaced structures relative to the non-displaced structure. These calculations show that the non-displaced structure has the lowest energy and represents the ground state of the system.

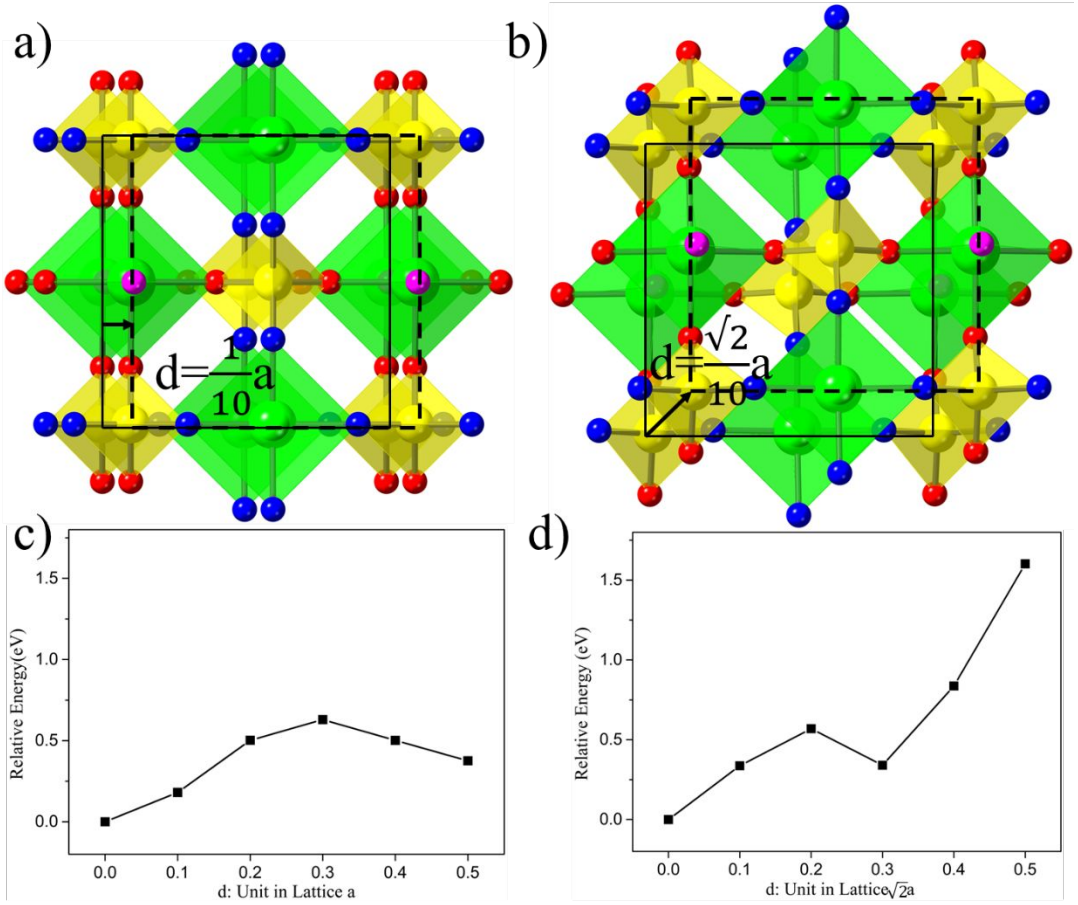

Figure 2. Illustration of the $VOPO_4$ layer displacement a) along the [100] direction and b) along the [110] direction. The solid black squares in a) and b) denote the original position of the second layer with respect to the first layer; the dashed black square denotes the displacement of the second layer. The corresponding energies as a function of displacement relative total energy as the reference of the original structure are shown in c) and d).

2.3 Ferrocene.

Ferrocene consists of two cyclopentadienyls, $C_5H_5^-$, rings with an iron ion located in the center between the two rings. Both experimental[55] and theoretical[56] investigations have consistently indicated that the eclipsed configuration, Figure 3 is energetically favored, exhibiting lower energy by 0.039 eV[55] and 0.027 eV,[56] respectively. Our calculations also support this trend, as we found that the eclipsed configuration is lower

in energy by 0.043 eV compared to the staggered configuration, aligning well with experimental observations. The small difference between our results and the prior theoretical[56] work can be attributed to the different DFT methods and basis set. In our study, we employed the GGA-PBE with D3 functional with plane wave basis set, while the previous work utilized the B3LYP hybrid functional with m6-31G(d). Considering the high computational resource requirements of the hybrid method, the GGA+U_D3 method is most suitable for our calculations. Additionally, given the periodic structure of the $VOPO_4$ in our study, the plane wave basis set is the better choice.

Table 2 presents the bond lengths of eclipsed configuration obtained from our calculations, along with other theoretical and experimental data. Rappoport et al.[57] showed that the GGA functional is generally more suitable for 3d element complexes, such as iron, whereas the hybrid functional is more suitable for 4d and 5d element complexes. Overall, these results demonstrate a high degree of consistency among different sources, thus validating the accuracy and reliability of our calculations.

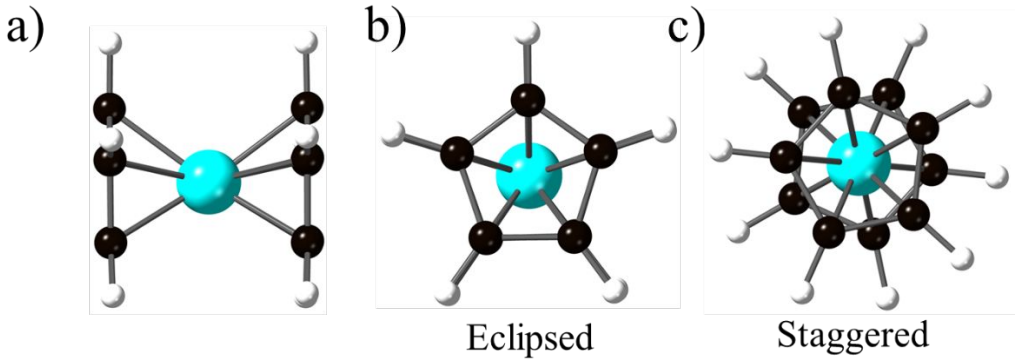

Figure 3. Side view (a) depiction eclipsed (b), and staggered (c) configurations of ferrocene. The iron is in cyan, carbon in black, and hydrogen in white.

Table 2. Optimized bond distances of eclipsed ferrocene from our calculations and other works. Unit in (Å).

Bond distance	**This work**	**B3LYP**[56]	**Experimental**[55]
Fe-C_5^*	1.634	1.670	1.660

Fe-C	2.039	2.065	2.064±0.003
C-C	1.434	1.428	1.440±0.002
C-H	1.086	1.082	1.104±0.006

*Denotes the distance from the iron atom to the center of the cyclopentadienyl ring.

3. Results

3.1 Configurations of ferrocene on vanadyl phosphate.

To thoroughly explore the possible configurations of ferrocene above the $VOPO_4$ layer, we considered all potential arrangements. In Section 2.3, we found that the eclipsed structure (E) is the lowest energy structure of the ferrocene in a vacuum. Although the staggered structure (S) of the isolated ferrocene molecule was 0.043 eV higher in energy than the eclipsed structure, the staggered arrangement remains a plausible arrangement during intercalation and is thus included in our analysis. In Figure 1, two distinct positions are identified for intercalation: between vanadium and vanadyl (V-VO), or between phosphorus and phosphorus (P/P). Taking into account the five-fold symmetry of ferrocene, we, therefore, consider two distinct orientations for the eclipsed ferrocene on the vanadium site. The left panel of Figure 4a, denoted the $E_{\perp}$-VO configuration, has the apical hydrogens of the eclipsed ferrocene cyclopentadienyl (C_5) rings pointing to the VO; the subscript '$\perp$' indicates that the plane of C_5 rings perpendicular to the $VOPO_4$ layer. The second to left panel denoted the $E_{\perp}$-V configuration has the apical hydrogens pointing to the V. The third possibility is shown in the third panel, in which the ferrocene is in the staggered configuration, for which there is only one structure, the $S_{\perp}$-V configuration. For both the eclipsed and staggered arrangements, we also examine the scenario in which the C_5 rings are parallel to the $VOPO_4$ layer, as depicted in the fourth panel of Figure 4a. Given the lack of orientation difference when the C_5 rings are parallel ('$\parallel$') to $VOPO_4$, whether near V or VO sites,

we simplify the nomenclature to $E_{\parallel}$-V for the eclipsed parallel arrangement and $S_{\parallel}$-V for the staggered parallel arrangement.

For each of these three structures $E_{\perp}$-V, $E_{\perp}$-VO, and $S_{\perp}$-V, we considered two orientations of the C_5 axis of the ferrocene. The first has the ferrocene axis parallel to [010], equivalent to [100], that we denote as a rotation angle of 0˚. The second has the ferrocene axis parallel to [110], equivalent to [-110],[1-10], and [-1-10]; we denote this rotation angle as 45 ˚, see Figure 4b. There are thus a total of six unique structures: $E_{\perp}$-V-0˚, $E_{\perp}$-V-45˚, $E_{\perp}$-VO-0˚, $E_{\perp}$-VO-45˚, $S_{\perp}$-V-0˚, and $S_{\perp}$-V-45˚.

For $E_{\parallel}$-V and $S_{\parallel}$-E, we also consider two possible rotation degree, focusing on the orientation of the carbon-hydrogen (C-H) bond, which is highlighted in the third and fourth panel of Figure 4b (carbon in orange and hydrogen in grey). If the C-H bond is parallel to the V-O bond, the rotation degree is 0˚. Alternatively, the angle between these two bonds is 45˚. There are three structures: $E_{\parallel}$-V-0˚, $E_{\parallel}$-V-45˚and $S_{\parallel}$-V-0˚. Therefore, there are a total of 9 (6+3) different structures on V-VO site.

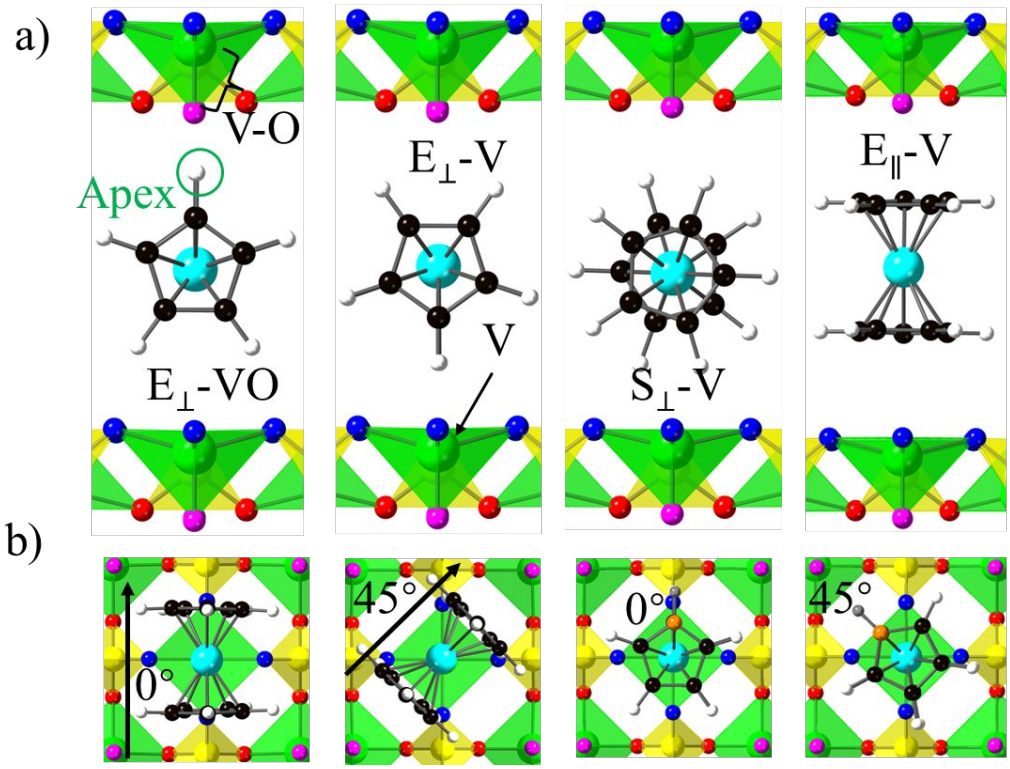

Figure 4. a) Different orientations of the cyclopentadienyl ring of ferrocene intercalation on the V/VO site, b) the different rotation degrees of ferrocene.

We turn now to ferrocene on the phosphorus site. Recall that phosphorus is tetrahedrally coordinated to oxygen. The red oxygen (Figure 1b) is along [010] direction and the blue oxygen (Figure 1b) is along [100] direction. Consequently, there are two distinct configurations when eclipsed ferrocene is located on a P site. In Figure 5, the left panel shows one configuration where the direction of C_5 axis of the ferrocene is along [010] direction (indicated by the orange arrow tail) and is parallel to the red oxygen atoms (marked by red arrow tail). This configuration is termed by $E_{\perp}$-P_{VO}. The P means the ferrocene located on P site, while the subscript 'vo' denotes that the direction of the apical hydrogen at the P site is the same as when the ferrocene was in the $E_{\perp}$-VO configuration. We labeled the configurations in this manner to maintain consistency with our previous notation for the V/VO sites. In the right panel of Figure 5, the C_5 axis of the ferrocene is perpendicular to the blue oxygen atoms (marked by the blue arrow). This configuration is labeled by $E_{\perp}$-P_V, where subscript 'v' indicates that the apical hydrogen at the P site is oriented similarly to the $E_{\perp}$-V configuration.

When considering the rotation of ferrocene, we find several identical configurations. For example, the $E_{\perp}$-P_{VO}-0˚ is equivalent to $E_{\perp}$-P_{V}-90˚, and $E_{\perp}$-P_{VO}-90˚ is the same as $E_{\perp}$-P_{V}-0˚. There is no distinction between $E_{\perp}$-P_{VO}-45˚ and $E_{\perp}$-P_{V}-45˚. For the staggered structure, there is no distinction between 0˚ and 90˚. There are thus only two staggered structures: $S_{\perp}$-P-0˚, and $S_{\perp}$-P-45˚. Furthermore, there are still three configurations on P site when C_5 rings parallel to $VOPO_4$ layer, namely, $E_{\parallel}$-P-0˚, $E_{\parallel}$-P-45˚ and $S_{\parallel}$-P-0˚. For more information about all of configurations, see Figure S1 and Table S1 in the SI.

In summary, there are nine unique configurations intercalated on the vanadium site ($E_{\perp}$-V-0˚, $E_{\perp}$-$V_{\perp}$-45˚, $E_{\perp}$-VO-0˚, $E_{\perp}$-VO-45˚, $S_{\perp}$-V-0˚, $S_{\perp}$-V-45˚, $E_{\parallel}$-V-0˚, $E_{\parallel}$-V-45˚and $S_{\parallel}$-V-0˚) and eight unique configurations on phosphorus site ($E_{\perp}$-P_{VO}-0˚, $E_{\perp}$-P_{V}-0˚, $E_{\perp}$-P_{VO}-45˚, $S_{\perp}$-P-0˚, $S_{\perp}$-P-45˚, $E_{\parallel}$-P-0˚, $E_{\parallel}$-P-45˚ and $S_{\parallel}$-P-0˚). The next step is to determine the total energy of each of these seventeen configurations.

3.2 Effect of the magnetic moment

Although in isolation neither the ferrocene nor the $VOPO_4$ layers has a magnetic moment, after intercalation, the magnetic moments of iron and vanadium are found to be 1.06 and 1.10 μB, respectively, due to charge transfer. Consequently, the total magnetic moment of these configurations can be either 0.04 μB or 2.16 μB depending on how they couple. However, the total energies were almost identical for the two cases. For instance, in the $E_{\perp}$-VO-0° configuration, the difference in total energy between the two magnetic moment states is only 2.6×10^{-3}meV/atom. Based on this finding, we conclude that the magnetic moment has a negligible effect on these configurations. In order to maintain consistency, we will utilize the total energies corresponding to a magnetic moment of 0.04 μB.

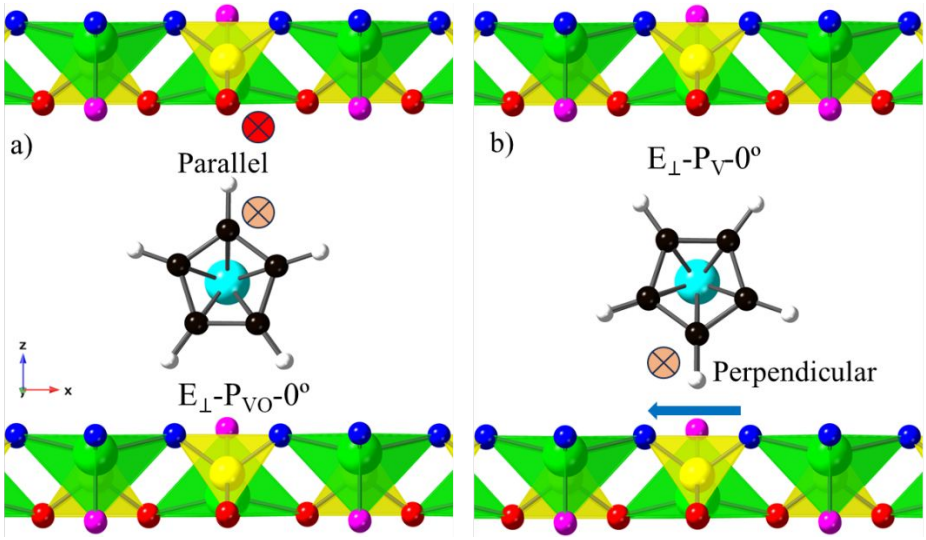

Figure 5. Ferrocene intercalation on the P/P site, a) $E_{\perp}$-P_{VO}-0° and b) $E_{\perp}$-P_{V}-0°, viewed along [010] direction. The orange junction sign is direction of axis of ferrocene, the purple junction sign is the direction of line connecting between red oxygens, and the gray arrow is the line connecting between blue oxygens.

3.3 The total energy comparison.

Figure 6 shows the energies of all 17 structures, relative to the lowest energy configuration, the $E_{\perp}$-V-45° structure. For precise total energy data, please refer to Table S2 in SI. Our site notation is based on the initial configurations. However, the final optimized structures differ from these initial configurations, some showing substantial distortion which we discuss below. For more details about the optimized structures, refer to Figure S2 in the SI.

In Figure 6, it is evident that there is a significant difference between configurations where the ferrocene rings are perpendicular to the $VOPO_4$ layers (the ⊥ arrangements) and those where the rings are parallel (the ∥ arrangements). Specifically, configurations with ferrocene rings parallel to the $VOPO_4$ layers have relative total energies that are 0.3 to 0.5 eV higher than those where the rings are perpendicular. This suggests that configurations with parallel orientation are less likely to happen due to their higher relative total energy. Therefore, our subsequent analysis will primarily concentrate on configurations with perpendicular orientation.

Considering the V-VO structures first, we see that the next lowest energy structure is the $S_{\perp}$-V-45°, with the $E_{\perp}$-VO-0°, $E_{\perp}$-VO-45°, and $S_{\perp}$-V-0° all having essentially the same energy. The highest energy is that of the $E_{\perp}$-V-0° structure. From the energy perspective, when the apical hydrogen faced the V-O, we observe that rotation does not significantly impact the total energy ($E_{\perp}$-VO-0° vs $E_{\perp}$-VO-45°), but it has a notable effect when the C-H apex faces the V (configurations $E_{\perp}$-V-0° vs $E_{\perp}$-V-45°). This behavior can be attributed to the distortion of the ferrocene structure and the resulting changes in van der Waals interactions, discussed below in Section 3.5.

Interestingly, we find that the initially staggered configuration $S_{\perp}$-V-0° exhibited the same total energy as the apex-faced V-O configuration, because the final relaxed structure shows that the ferrocene is actually not staggered but eclipsed, and thus the relaxed structure is the same as $E_{\perp}$-VO-0°. Moreover, although the ferrocene with a rotation degree of 45° can be staggered, the total energy is 0.05 eV higher than the eclipsed configuration with a 45° rotation degree. Therefore, the Ferrocene adopts an eclipsed over the staggered arrangement intercalated between V and V-O sites. Because of unique configurations of ferrocene intercalated between phosphorus is reduced from 8 to 6.

More importantly, we also examine whether temperature significantly affects the most stable configuration. To this end, we perform vibrational frequency calculations. Given that these calculations are both time-intensive and computationally demanding, we limit our analysis to the two lowest energy configurations, $E_{\perp}$-V-45° and $S_{\perp}$-V-45°. See calculation results in Figure S3 in SI. Our findings indicate that at room temperature, the vibrational contributions to the Gibbs free energy are quite similar, with energy differences of 0.045 eV and 0.075 eV at 0K and 298K, respectively. Since the ranking of configurations remains unchanged and the contributions to the vibrational free energy are similar for the two structures, we conclude that our analyses of zero-temperature results can be expected to be valid at room temperature.

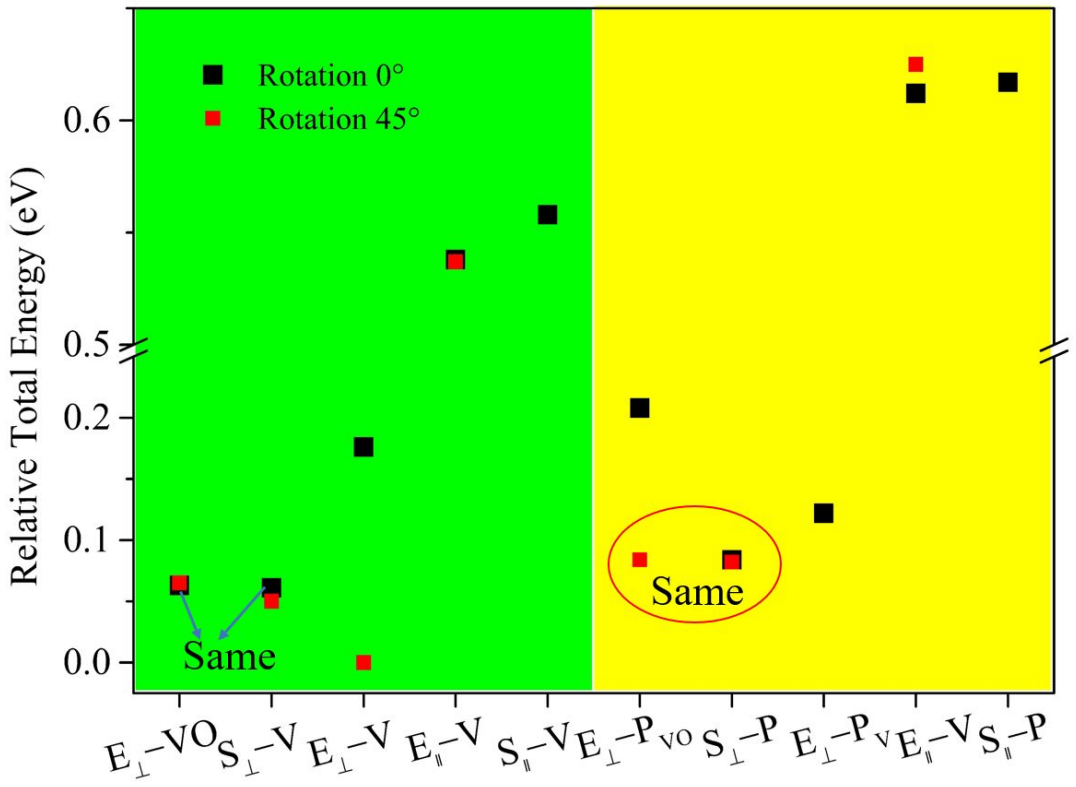

Figure 6. The relative total energy of 17 different configurations. The reference is $E_{\perp}$-V-45°. The green region means the ferrocene located on the V/VO site, while yellow region means the ferrocene located on the P/P site.

The lowest energy for the ferrocene over the P site is for the $S_{\perp}$-P-0°, $S_{\perp}$-P-45°, and $E_{\perp}$-P_{VO}-45°, each of which has the same energy. This is attributable to the fact that these three configurations have identical final relaxed configurations. Unlike $E_{\perp}$-P_{VO}-0° and $E_{\perp}$-P_{V}-0°, which retained the eclipsed ferrocene arrangement, these three configurations show that the orientation of ferrocene is rotated approximately 20° degree relative to the [010] direction in the (001) plane, and is simultaneously accompanied by cyclopentadienyl rings structure deviating from an eclipsed or staggered conformations and settling to a gauche arrangement in which there is partial staggering (Figure 7). We therefore denote these three configurations as $G_{\perp}$-P-20°, where G represents a gauche arrangement, P is a ferrocene located on the P/P site and 20° represents the ferrocene C_5 axis is rotated relative to the [010] direction. Furthermore, it is noteworthy that the $G_{\perp}$-P-20° configuration exhibits lower energies compared to the $E_{\perp}$-P_{VO}-0° and $E_{\perp}$-P_{V}-0° configurations. This result implies that the

ferrocene tends to adopt the structures depicted in Figure 7 rather than the eclipsed configuration when located on the P/P site. Thus, the total number of unique configurations of ferrocene intercalated between phosphorus is reduced from 8 to 6.

When we compare the total energy of ferrocene intercalated on V/VO and P/P, most configurations have lower total energy on V/VO than on P/P, except the $E_{\perp}$-V-0° configuration. Also, the lowest total energy is the $E_{\perp}$-V-45° configuration, which is on the V/VO site. Therefore, we conclude that the ferrocene prefers to reside on the V/VO site rather than on the P/P site. This can be attributed to the signficant charge transfer between vanadium and iron, as is discussed in section 3.4. All eight (8+6) optimized structures are shown in SI in VASP POSCAR file style.

3.4 The solvent effect.

To assess the influence of solvent in our calculations, we employ an implicit solvation model[41–43] where we compute the total energies of the two most stable configurations namely $E_{\perp}$-V-45° and $S_{\perp}$-V-45°. The analysis revealed only minimal variations in total energy differences between the vacuum and solvation states (0.051 eV and 0.044 eV, respectively), suggesting a limited impact of solvent on our findings and the total energy order remaining same. Consequently, this work primarily focuses on the contributions of ferrocene.

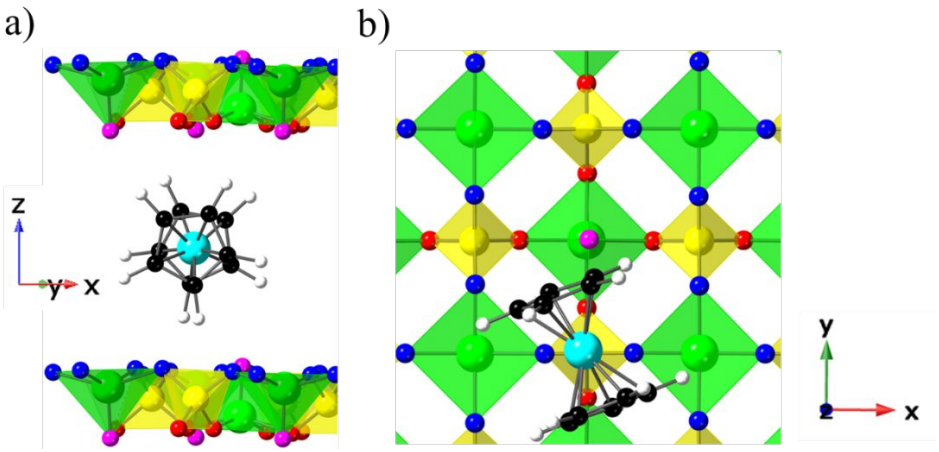

Figure 7. The most stable, gauche, configuration of ferrocene intercalated between phosphorus and phosphorus, viewed a) along the [-120] direction and b) along the [001] direction.

3.5 Charge density difference maps.

In Section 3.3, we explored the preference of ferrocene to intercalate onto the vanadium/vanadyl site rather than onto the phosphorus site within the $VOPO_4$ structure. Upon intercalation, ferrocene is oxidized from Fe^{2+} to Fe^{3+} and the host is partially reduced from V^{5+} to V^{4+}.[27] To gain insights into the underlying mechanisms, we characterize the charge distribution after ferrocene intercalation.

We firstly perform Bader charge analysis[58–61]on the eight energetically distinct configurations identified in the energy and structure analysis. The results demonstrate that the charge on the ferrocene is approximately +0.95, with only slight variations among the different configurations, please refer to Figure S4 in SI. Although Bader charges cannot be directly mapped to experimental charges, the sign and magnitude are consistent with the experimental data.[27]

To visualize the charge transfer, we generate charge density difference maps for each structure. These maps are obtained by subtracting the charge density of the ferrocene-$VOPO_4$ complex from the isolated ferrocene and the $VOPO_4$ layer at the corresponding positions. In Figure 8a and Figure 8b, charge accumulations are observed

on vanadium atoms, while charge deficits are observed on iron atoms, regardless of whether ferrocene is located above vanadium or phosphorus. We only show the lowest total energy configurations for intercalation at vanadium and phosphorus respectively; the other six configurations are shown in Figure S5 in the SI. Interestingly, in Figure 8b showing ferrocene located above phosphorus we observe charge accumulation on the left vanadium atom (see red circle). However, from a symmetry perspective, the right vanadium atom (see blue circle) should have the same effect as the left one as it is in an equivalent position. Upon applying charge accumulation to the right vanadium rather than the left, the total energy is essentially the same, differing by only 3.9×10^{-2} meV/atom. For consistency in our subsequent analyses, we consider structures in which the charge accumulation is on the left vanadium. A detailed analysis on this charge accumulation phenomenon can be found in Figure S6 and Table S3 in SI.

To gain further insights into charge accumulation, we analyze a [001] plane in the system through four vanadium atoms. This plane allows us to distinguish which vanadium atoms exhibit charge accumulation and which ones do not. Figure 9 illustrates this plane and clearly shows that ferrocene is located where vanadium charge accumulation occurs. However, neither of the remaining three vanadium atoms nor any of the phosphorus exhibit any charge transfer. While intercalated on phosphorus, it shows a similar charge difference, as shown in Figure S7 in the SI. In short, charge accumulation in the vanadyl phosphate layer localizes on individual sites and ferrocenium prefers to locate on the reduced V/VO site instead of P/P site, maximizing electrostatic interactions.

Also, as mentioned in Section 3.2, both iron and vanadium exhibit magnetic moments, resulting in a dipolar coupling between them.[27,62,63] To elucidate the influence of this effect on the system's total energy, calculations were performed with and without spin-polarization. For the configurations $E_{\perp}$-V-45° (the most energetically stable at the V/VO site) and $G_{\perp}$-P-20° (the most energetically stable at the P/P site), the energy difference is 0.084 eV with spin-polarization, compared to a mere 0.023 eV without.

This significant reduction in energy difference for the non-spin-polarized calculations highlights the pronounced impact of dipolar coupling in the $E_{\perp}$-V-45° configuration.

In short, our calculations conclude that the reason that ferrocene prefers to stay on vanadium rather than phosphorus is due to charge transfer and the stronger dipolar coupling. The charge localization on vanadium facilitates a favorable interaction between ferrocenium and the reduced vanadium site, contributing to the stability of the ferrocene intercalated system.

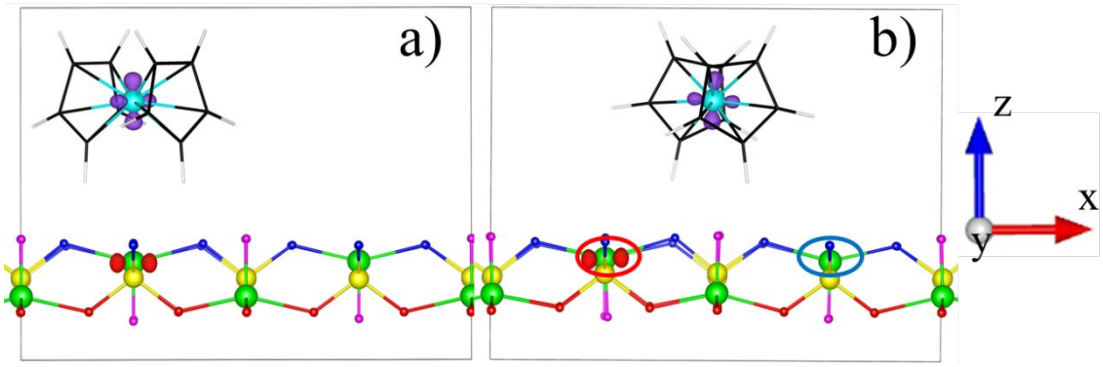

Figure 8. Charge density maps of a) $E_{\perp}$-V-45°, and b) $G_{\perp}$-P-20°. The red region means the charge accumulation, while the violet region means the charge reduction. The issovalue is 0.04 e/Å^3. All of the pictures viewed along [010] direction.

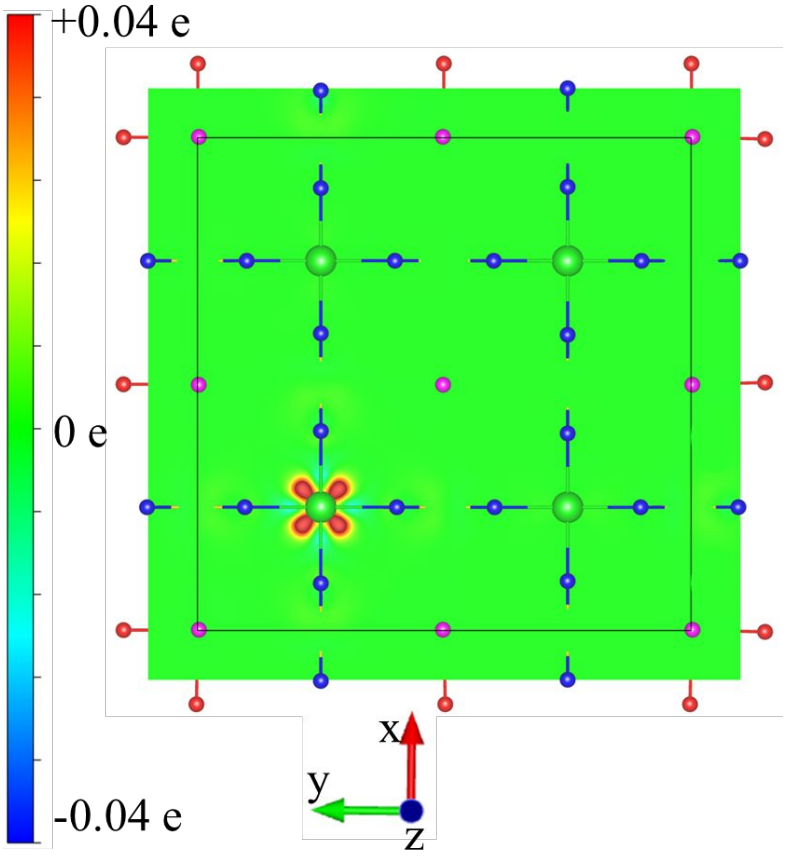

Figure 9. Charge density difference map built by the four vanadium atoms, viewed along [001] direction; the ferrocene, which sits on top of the V at the bottom left has been omitted due to the clarity. The red region means the charge accumulation. The black box indicated the unit cell. The isovalue is 0.04 e/Å^3.

3.6 Electron localization function and hirshfeld surface anaylsis.

The analysis presented in Figure 6 showed the variation of the system's total energy based on the orientation and rotation of the cyclopentadienyl ring in ferrocene intercalated between vanadium in one layer and the vanadyl oxygen in the other. The primary objective of this section is to gain an understanding of the underlying mechanisms driving this variation. When the hydrogen apex from the cyclopentadienyl ring faced the vanadyl oxygen, namely, $E_{\perp}$-VO configurations, the distortion of the ferrocene remains minimal for in-plane rotations of both 0° and 45°. However, substantial distortion of ferrocene occurs for $E_{\perp}$-V configurations (see Figure 10). For

rotations of 0° and 45°, the cyclopentadienyl rings bend, opening at the apical hydrogens facing the V side. To determine the extent of bending, we measured the dihedral angle between the rings (Table 3).[64] A higher dihedral angle in the $E_{\perp}$-V configurations indicates greater bending. (See Figures 10c and 10d). This distortion of ferrocene has two possible origins. Firstly, it arises from the interactions between the apical hydrogen atoms in the cyclopentadienyl ring and the VO_5 oxygen atoms, leading to van der Waals forces that induce the distortion of the ferrocene cyclopentadienyl ring. Secondly, the distortion might arise from the enhanced electrostatic interactions upon bending between the cationic component ($[Cp_2Fe]^+$) and the anionic counterpart ($[VO_5]^-$), a phenomenon which can be described within the framework of the polarizable ion model (PIM).[65]

With regards to the first possible origin, the distortion of the ferrocene tends to increase the total energy, whereas the van der Waals interactions tend to decrease it. To quantitatively assess the impact of ferrocene distortion, we isolated the ferrocene moiety from the relaxed structure and conducted a single-point calculation, comparing it to the original ferrocene, see Table 3. Remarkably, the ferrocene extracted from the $E_{\perp}$-V configurations exhibits the highest relative energy, aligning with our initial assumptions. In other words, $E_{\perp}$-V-0° possesses a higher total energy than $E_{\perp}$-VO-0° primarily due to the dominance of ferrocene distortion energy over the reduction in van der Waals energy. However, as the ferrocene rotates to 45° degrees, the van der Waals interactions strengthen, leading to a lower total energy of the system.

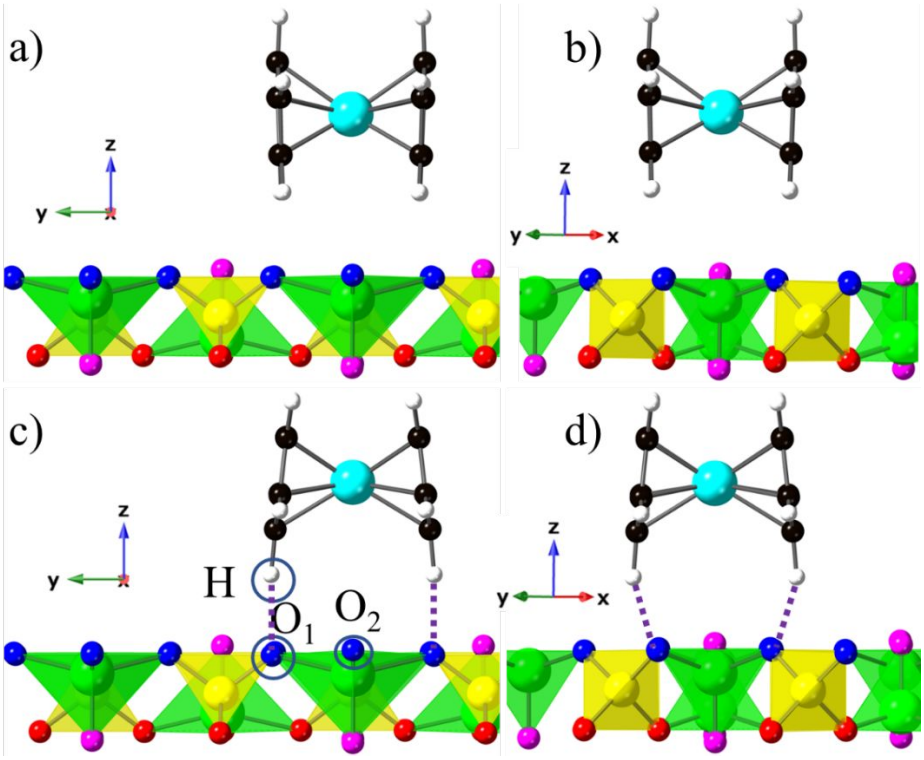

Figure 10. a) $E_{\perp}$-VO-0° configuration, viewed along [100] direction; b) $E_{\perp}$-VO-45° configuration, viewed along [110] direction; c) $E_{\perp}$-V-0° configuration, viewed along [100] direction; and d) $E_{\perp}$-V-45° configuration, viewed along [110] direction. The purple dashed lines mean the vdW interactions, which are proven in Figure 11.

Table 3. The relative total energy in eV of ferrocene extracted from the $VOPO_4$ layer compared to that of pure ferrocene.

Name	Dihedral Angle (°)	Relative Total Energy
Pure Eclipsed Ferrocene	0	0
$E_{\perp}$-VO-0° Ferrocene	2.98	+0.15
$E_{\perp}$-VO-45° Ferrocene	2.34	+0.15
$E_{\perp}$-V-0° Ferrocene	13.49	+0.21
$E_{\perp}$-V-45° Ferrocene	12.04	+0.20

To underscore the significance of the van der Waals correction, we perform calculations on the four configurations both with and without the D3 correction. The dihedral angles of ferrocene exhibit minimal deviation irrespective of the presence of the D3 correction, indicating that the optimized geometries are very similar in both scenarios; see Table S4 in SI for more details. Nonetheless, upon detailed examination of the total energies present in Table 4, discrepancies become evident. The configuration $E_{\perp}$-V-45° is identified as the most energetically stable in the presence of the D3 correction, whereas the $E_{\perp}$-VO-0° and $E_{\perp}$-VO-45° configuration are most stable without it. Furthermore, the energy difference between $E_{\perp}$-V-0° and $E_{\perp}$-V-45° increases (0.067 eV to 0.176 eV) when the D3 correction is applied, suggesting a stronger van der Waals force in the $E_{\perp}$-V-45° configuration. In summary, van der Waals forces play a pivotal role in the distortion of ferrocene.

Table 4. Relative total energy comparison: with D3 (Reference: $E_{\perp}$-V-45°) versus without D3 (Reference: $E_{\perp}$-VO-0°) in eV.

Name	With van der Waals	Without van der Waals
$E_{\perp}$-VO-0°	+0.063	0
$E_{\perp}$-VO-45°	+0.065	+0.001
$E_{\perp}$-V-0°	+0.176	+0.118
$E_{\perp}$-V-45°	0	+0.051

To illustrate the changes in the strength of the van der Waals interactions more clearly, we plotted the electron localization function (ELF)[48] associated with the interaction between hydrogen atoms and oxygen atoms, Specifically, O_1 and O_2, the two closest oxygens to the apical hydrogen from cyclopentadienyl ring, see Figure 10c. The ELF, a scalar function ranging from 0 to 1, provides insight into the probability density of locating a pair of electrons with the same spin near a reference electron pair. Koumpouras[66] *et al.* reported that values above 0.7 indicate electron localization in the

core, covalent bonding, or lone pair regions; values between 0.7 and 0.2 suggest electron-gas behavior or the presence in metallic bonds; values below 0.2 indicate delocalized electrons involved in non-covalent bonds. Furthermore, if the ELF is less than 0.2 but not zero and exhibits a V-shaped pattern, it signifies van der Waals interaction. An ELF value approaching zero (less than 0.01) indicates an ionic bond. In Figure 11a, the ELF analysis of the $E_{\perp}$-V-0° configuration clearly shows that the hydrogen and O_1 atoms possess a non-zero value, indicative of the presence of van der Waals interactions. However, no van der Waals interaction is observed between the hydrogen atom and O_2, as evidenced by the zero value at the minimum point. By contrast, the $E_{\perp}$-V-45° configuration in Figure 11b shows that there are van der Waals interactions between the hydrogen atom and both O_1 and O_2. Thus, our findings support the notion that this configuration exhibits the lowest total energy due to stronger van der Waals interactions.

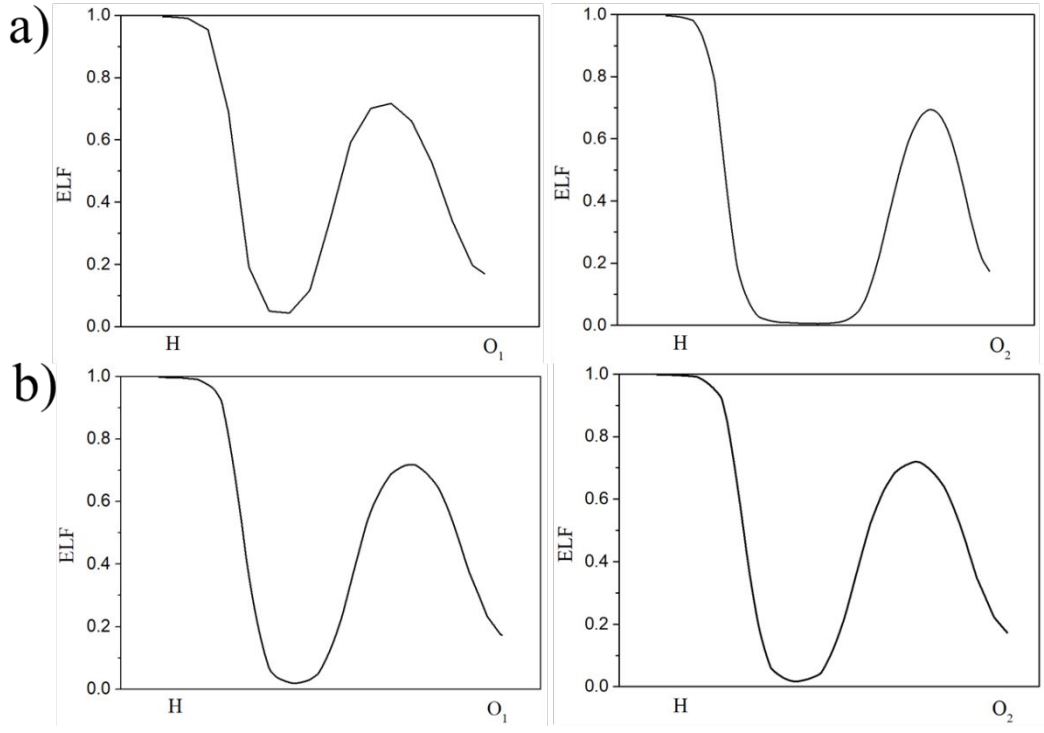

Figure 11. The linear profile ELF of H to O_1 and O_2, a) $E_{\perp}$-V-0° and b) $E_{\perp}$-V-45°.

Turning to the second possible origin, the polarized ion model, we constructed a supercell in the 'c' direction, as illustrated in Figure 12a. This supercell comprises two distinct layers: one intercalated with ferrocene and the other without ferrocene. According to the principles of the polarizable ion model, the observed bending of ferrocene can be traced back to intensified electrostatic interactions with the VO_5. Within two distinct layers, iron may engage in charge transfer with either the bottom or the top VO_5 layer. In scenarios where charge transfers with the bottom layer, the ferrocene exhibits a distortion oriented facing the V side, and conversely, when it's with the top layer, the distortion is towards the V-O side. However, it reveals charge transfer exclusively with the bottom layer after relaxation, resulting in ferrocene consistently facing the V side, as clearly shown in Figures 12b. We only show $E_{\perp}$-V-45° here due to the simliar results, the other $E_{\perp}$-VO-0°, $E_{\perp}$-VO-45° and $E_{\perp}$-V-0° are shown in Figure S8 in SI.

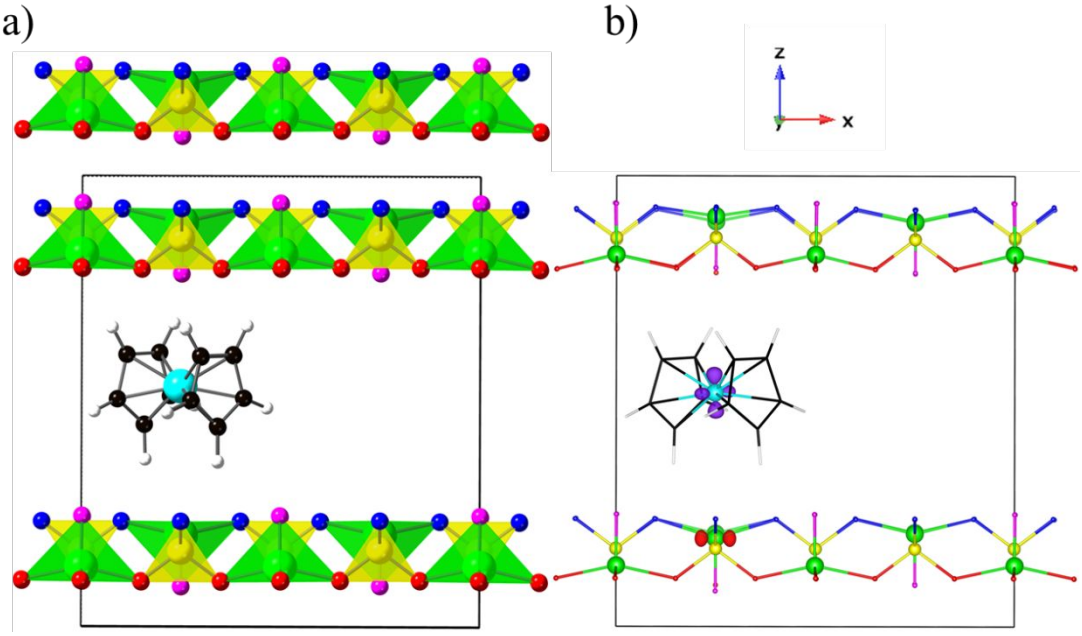

Figure 12. Supercell structure of a) $E_{\perp}$-V-45° configuration, and b) the corresponding charge density difference map, the isovalue is 0.04 e/Å^3, viewed along [010] direction. The black box is the supercell structure.

Despite these findings, the definitive functioning of the PIM remains uncertain. To gain further clarity, we employed the Hirshfeld surface analysis[50] as used in Malischewski *et al.*[65] work. In our supercell study, the $E_{\perp}$-VO-0° configuration reveals a slight electron density between the bottom vanadium atom, evident in Figure 13a. The $E_{\perp}$-VO-45° configuration displays a similar pattern, as shown in Figure S9a of the SI. However, $E_{\perp}$-V-45° (Figure 13b) and $E_{\perp}$-V-0° (Figure S9b in the SI) reveal a denser electron presence between iron and the VO_5 layer, with $E_{\perp}$-V-45° the densest. This stronger electron density between the iron and the V-site in the $E_{\perp}$-V-45° configuration supports the theory that ferrocene maintains a strong electrostatic interaction with the localized charge in the VO_5 layer. For other orientations of Hirshfeld surface analysis, see Figure S10 in SI. Consequently, it can be inferred that the PIM also plays a role in causing the observed bending of ferrocene.

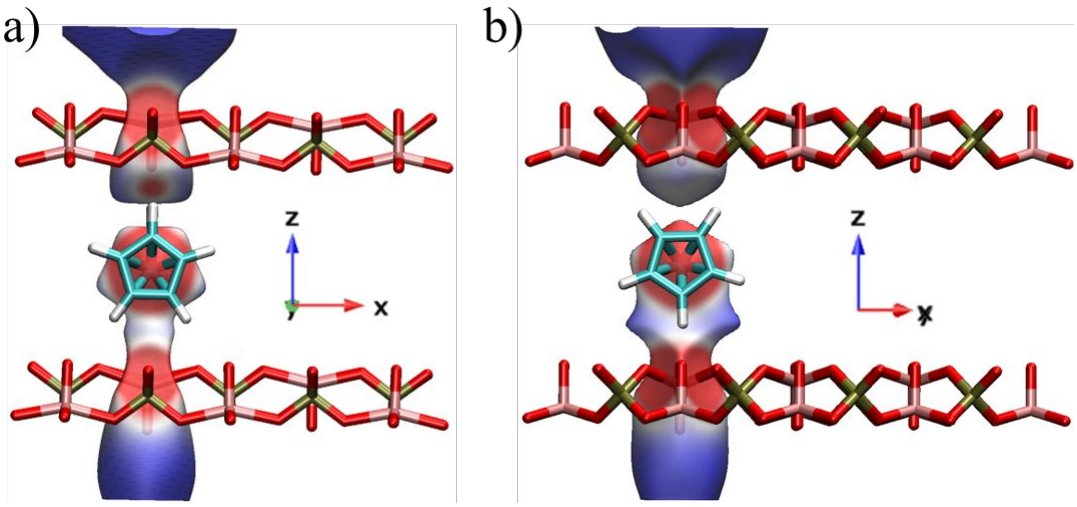

Figure 13. Hirshfeld surface analysis of a) $E_{\perp}$-VO-0°, viewed along [010] direction, and b) $E_{\perp}$-V-45°, viewed along [-110] direction. Red means high electron density, white means medium electron density and blue means low electron density.

4. Discussion and Conclusions.

In this study, DFT calculations using GGA+U_D3 accurately reproduced experimental observations for ferrocene intercalation into $VOPO_4$. The calculated bond

lengths and stability of the eclipsed configuration of ferrocene, lattice expansion, Bader charge analysis, and charge density differences all agreed well with experimental data. Thus, the DFT method reliably captures the structural, energetic, and charge-related aspects of the intercalation process, while providing new insights atomic level interactions between the ferrocenium guest and the $VOPO_4$ host

We investigated the 17 possible configurations of ferrocene intercalation into the $VOPO_4$ layer. By optimizing these configurations, we found that there are only 14 distinct configurations because some of them have the same final equilibrated structures. From the perspective of relative total energies, our calculations revealed four key findings. First when ferrocene is intercalated into $VOPO_4$, the cyclopentadienyl rings are more likely to orient perpendicularly rather than parallel to the $VOPO_4$ layers. Second, Ferrocene's preference to reside on V/VO rather than on P is attributable to charge transfer between iron and vanadium and stronger dipolar coupling effect. Third, the most stable configuration is $E_{\perp}$-V-45°, which exhibits stronger van der Waals interactions between hydrogens of the cyclopentadienyl ring and oxygens of the VO_5 group, as supported by the electron localization function (ELF) analysis. Fourth, ferrocene adopts an eclipsed conformation intercalated between vanadium and oxygen-vanadium, while gauche conformation between phosphorus and phosphorus. Furthermore, based on structural analysis, we observe that the ferrocene bends in both $E_{\perp}$-V-45° and $E_{\perp}$-V-0°. This distortion stems from two factors. Firstly, the apical hydrogen from the cyclopentadienyl rings exhibits a van der Waals interaction with the oxygen in VO_5. Secondly, ferrocene demonstrates a stronger electrostatic anion-cation interaction with vanadyl. This observation is corroborated by the Hirshfeld surface analysis.[50]

Guest transport within host lattices is a critical mechanistic step in ion exchange, ion and molecular storage and battery applications.[67] The results show we can anticipate that the migration behavior of ferrocene in the layered host is quite complex. At different locations in the $VOPO_4$ layers, for instance, the V/VO site vs. the P/P site, the

ferrocene configuration alters, changing the arrangement of the cyclopentadienyl ring and the rotation of the ferrocene molecule itself. The results of the present study will enable molecular-level studies of complex ion transport processes, providing a valuable complement to phase field modeling of macroscopic behavior.[68,69] In the future, we will carry out these structures and use nudged elastic band calculations[70,71] to elucidate the energy barriers associated with the diffusion of ferrocene on the $VOPO_4$ layer, providing insights into the dynamics and kinetics of ferrocene intercalation, further enhancing our understanding of the intercalation process.

However, several factors remain unexplored in our study. Firstly, the solvent effect has not been fully considered. Given the aqueous chemical environment, it is reasonable to assume that the vacancies in $VOPO_4$ would be filled with solvent molecules. Although our results have demonstrated that the binding energy between ferrocene and $VOPO_4$ is stronger than that between water and $VOPO_4$, the solvent effect still warrants further investigation. Therefore, we plan to employ both explicit and implicit solvation models[41–43] in future work to comprehensively account for solvent effects. Secondly, this paper assumes a ferrocene occupancy ratio of 0.125, consistent with the findings of from experimental study.[30] However, other research[26] suggests that this ratio could be 0.21 Consequently, we aim to adjust the number of ferrocene molecules in our system in future studies to more fully explore the intercalation process.

Acknowledgments

This work was supported, in part, by the Division of Materials Research (DMR) at the National Science Foundation (NSF) via DMR-1904596 (D.R.T.),

CRediT author statement.

Yuan Liu: Conceptualization, Methodology, Software, Writing – Original Draft, Visualization; **An T. Ta:** Conceptualization, Supervision, Validation; **Seaton Ullberg:** Methodology, Validation; **Jiahui Liu:** Conceptualization, Investigation; **Daniel R. Talham:** Conceptualization, Writing - Review & Editing, Supervision; **Simon R. Phillpot:** Conceptualization, Validation, Writing - Review & Editing and Supervision.

References:

1 Y. Zhu, Y. Qian, Z. Ju, Y. Ji, Y. Yan, Y. Liu and G. Yu, *ACS Nano*, 2020, **14**, 13824–13833.

2 Y. Zhang, E. Huixiang Ang, Y. Yang, M. Ye, W. Du, C. Chao Li, Y. F. Zhang, Y. Yang, M. H. Ye, W. C. Du, C. C. Li and E. H. Ang, *Adv. Funct. Mater.*, 2021, **31**, 2007358.

3 M. S. Whittingham, C. Siu and J. Ding, *Acc. Chem. Res.*, 2018, **51**, 258–264.

4 H. Shi, Z. Jia, W. Wu, X. Zhang, X. Liu and X. Sun, *Chem. – A Eur. J.*, 2020, **26**, 8190–8204.

5 M. Faizan, Y. Li, R. Zhang, X. Wang, P. Song and R. Liu, *Chinese J. Chem. Eng.*, 2022, **43**, 297–315.

6 F. Rüther, R. Machado, E. Gioria, S. L. Kunz, K. Wittich, P. Löser, M. Geske, S. A. Schunk, R. Glaum and F. Rosowski, *ACS Catal.*, 2023, **13**, 3295–3307.

7 M. Nakamura, *J. Catal.*, 1974, **34**, 345–355.

8 M. Di Serio, M. Cozzolino, R. Tesser, P. Patrono, F. Pinzari, B. Bonelli and E. Santacesaria, *Appl. Catal. A Gen.*, 2007, **320**, 1–7.

9 F. Puzzo, N. Capece, L. Setti, G. Pavarelli, J. De Maron, T. Tabanelli and F. Cavani, *Appl. Catal. A Gen.*, 2023, **661**, 119243.

10 X. Li, A. M. Elshahawy, C. Guan and J. Wang, *Small*, 2017, **13**, 1701530.

11 M. Shao, J. Deng, F. Zhong, Y. Cao, X. Ai, J. Qian and H. Yang, *Energy Storage Mater.*, 2019, **18**, 92–99.

12 Y. Shi, H. Zhou, S. Britto, I. D. Seymour, K. M. Wiaderek, F. Omenya, N. A. Chernova, K. W. Chapman, C. P. Grey and M. S. Whittingham, *Electrochem. commun.*, 2019, **105**, 106491.

13 H. Wu, Y. Chen, T. Wen, L. Chen, X. Pu and Z. Chen, *Batteries*, 2023, **9**, 56.

14 J. Liao, Y. Han, Z. Zhang, J. Xu, J. Li and X. Zhou, *ENERGY Environ. Mater.*, 2021, **4**, 178–200.

15 X. Li, Z. Chen, Y. Yang, S. Liang, B. Lu and J. Zhou, *Inorg. Chem. Front.*, 2022, **9**, 3986–3998.

16 K. Zhu, Z. Sun, P. Liu, H. Li, Y. Wang, K. Cao and L. Jiao, *J. Energy Chem.*, 2021, **63**, 239–245.

17 L. Peng, Y. Zhu, X. Peng, Z. Fang, W. Chu, Y. Wang, Y. Xie, Y. Li, J. J. Cha and G. Yu, *Nano Lett.*, 2017, **17**, 6273–6279.

18 F. Zhou, M. Cococcioni, K. Kang and G. Ceder, *Electrochem. commun.*, 2004, **6**, 1144–1148.

19 J. S. O. Evans, S. J. Price, H. V. Wong and D. O'Hare, *J. Am. Chem. Soc.*, 1998, **120**, 10837–10846.

20 Y. Zhu, Y. Ji, Z. Ju, K. Yu, P. J. Ferreira, Y. Liu and G. Yu, *Angew. Chemie Int. Ed.*, 2019, **58**, 17205–17209.

21 Y. Zhu, Y. Qian, Z. Ju, L. Peng and G. Yu, *Nano Lett.*, 2018, **18**, 6071–6075.

22 C. F. Ferreira, E. E. Pérez-Cordero, K. A. Abboud and D. R. Talham, *Chem. Mater.*, 2016, **28**, 5522–5529.

23 Y. Lu, P. Zhang, F. Wang, K. Zhang and X. Zhao, *Electrochim. Acta*, 2018, **274**, 359–369.

24 P. Stein, Y. Zhao and B. X. Xu, *J. Power Sources*, 2016, **332**, 154–169.

25 X. yu Zhang, H. Sen Chen and D. Fang, *Int. J. Mech. Sci.*, 2020, **169**, 105323.

26 G. Matsubayashi and S. Ohta, *Chem. Lett.*, 1990, 19, 787–790.

27 A. Davidson, G. Villeneuve, L. Fournes and H. Smith, *Mater. Res. Bull.*, 1992, **27**, 357–366.

28 S. Okuno and G. Matsubayashi, *Chem. Lett.*, 1993, **22**, 799–802.

29 L. Beneš, K. Melánová, J. Svoboda and V. Zima, *J. Incl. Phenom. Macrocycl. Chem. 2012 731*, 2012, **73**, 33–53.

30 E. Rodríguez-Castellón, A. Jiménez-Ĺópez, M. Martínez-Lara and L. Moreno-Real, *J. Incl. Phenom.*, 1987, **5**, 335–342.

31 G. Kresse and J. Hafner, *Phys. Rev. B*, 1993, **47**, 558.

32 G. Kresse and J. Furthmüller, *Phys. Rev. B*, 1996, **54**, 11169–11186.

33 J. P. Perdew, K. Burke and M. Ernzerhof, *Phys. Rev. Lett.*, 1996, **77**, 3865–3868.

34 P. E. Blöchl, *Phys. Rev. B*, 1994, **50**, 17953.

35 G. Kresse and D. Joubert, *Phys. Rev. B*, 1999, **59**, 1758–1775.

36 S. L. Dudarev, G. A. Botton, S. Y. Savrasov, C. J. Humphreys and A. P. Sutton, *Phys. Rev. B*, 1998, **57**, 1505.

37 B. Stahl and T. Bredow, *J. Comput. Chem.*, 2020, **41**, 258–265.

38 D. Sun, M. Okubo and A. Yamada, *Chem. Sci.*, 2021, **12**, 4450–4454.

39 S. Grimme, J. Antony, S. Ehrlich and H. Krieg, *J. Chem. Phys.*, 2010, **132**, 154104.

40 W. Hujo and S. Grimme, *Phys. Chem. Chem. Phys.*, 2011, **13**, 13942.

41 K. Mathew, R. Sundararaman, K. Letchworth-Weaver, T. A. Arias and R. G. Hennig, *J. Chem. Phys.*, 2014, **140**, 084106.

42 K. Mathew, V. S. C. Kolluru, S. Mula, S. N. Steinmann and R. G. Hennig, *J. Chem. Phys.*, 2019, **151**, 234101.

43 S. M. R. Islam, F. Khezeli, S. Ringe and C. Plaisance, *J. Chem. Phys.*, 2023, **159**, 234117.

44 D. M. Bylander, L. Kleinman and S. Lee, *Phys. Rev. B*, 1990, **42**, 1394–1403.

45 M. P. Teter, M. C. Payne and D. C. Allan, *Phys. Rev. B*, 1989, **40**, 12255–12263.

46 V. Wang, N. Xu, J.-C. Liu, G. Tang and W.-T. Geng, *Comput. Phys. Commun.*, 2021, **267**, 108033.

47 E. a crystal and molecular structures program for Mac and Windows. CrystalMaker Software Ltd, Oxford, Images and video generated using CrystalMaker, www.crystalmaker.com.

48 A. Savin, R. Nesper, S. Wengert and T. F. Fässler, *Angew. Chemie Int. Ed. English*, 1997, **36**, 1808–1832.

49 K. Momma and F. Izumi, *J. Appl. Crystallogr.*, 2011, **44**, 1272–1276.

50 M. A. Spackman and D. Jayatilaka, *CrystEngComm*, 2009, **11**, 19–32.

51 T. Lu and F. Chen, *J. Comput. Chem.*, 2012, **33**, 580–592.

52 W. Humphrey, A. Dalke and K. Schulten, *J. Mol. Graph.*, 1996, **14**, 33–38.

53 T. M. Project, , DOI:10.17188/1193783.

54 H. Tietze, *Aust. J. Chem.*, 1981, **34**, 2035.

55 A. Haaland, J. E. Nilsson, T. Olson and T. Norin, *Acta Chem. Scand.*, 1968, **22**, 2653–2670.

56 N. Mohammadi, A. Ganesan, C. T. Chantler and F. Wang, *J. Organomet. Chem.*, 2012, **713**, 51–59.

57 D. Rappoport, N. R. M. Crawford, F. Furche and K. Burke, in *Encyclopedia of Inorganic Chemistry*, Wiley, Chichester, UK, 2005, vol. 123, p. 104101.

58 M. Yu and D. R. Trinkle, *J. Chem. Phys.*, 2011, **134**, 064111.

59 G. Henkelman, A. Arnaldsson and H. Jónsson, *Comput. Mater. Sci.*, 2006, **36**,

354–360.

60 E. Sanville, S. D. Kenny, R. Smith and G. Henkelman, *J. Comput. Chem.*, 2007, **28**, 899–908.

61 W. Tang, E. Sanville and G. Henkelman, *J. Phys. Condens. Matter*, 2009, **21**, 084204.

62 K. J. Griffith and J. M. Griffin, in *Comprehensive Inorganic Chemistry III*, Elsevier, 2023, vol. 1–10, pp. 282–329.

63 K. Chen, Y. Sun and G. Hou, in *Comprehensive Inorganic Chemistry III*, Elsevier, 2023, vol. 1–10, pp. 471–513.

64 J. C. Green, *Chem. Soc. Rev.*, 1998, **27**, 263.

65 M. Malischewski, M. Adelhardt, J. Sutter, K. Meyer and K. Seppelt, *Science (80-.).*, 2016, **353**, 678–682.

66 K. Koumpouras and J. A. Larsson, *J. Phys. Condens. Matter*, 2020, **32**, 315502.

67 A. Sood, A. D. Poletayev, D. A. Cogswell, P. M. Csernica, J. T. Mefford, D. Fraggedakis, M. F. Toney, A. M. Lindenberg, M. Z. Bazant and W. C. Chueh, *Nat. Rev. Mater. 2021 69*, 2021, **6**, 847–867.

68 R. B. Smith, E. Khoo and M. Z. Bazant, *J. Phys. Chem. C*, 2017, **50**, 18.

69 L. Hong, L. Li, Y.-K. Chen-Wiegart, J. Wang, K. Xiang, L. Gan, W. Li, F. Meng, F. Wang, J. Wang, Y.-M. Chiang, S. Jin and M. Tang, *Nat. Commun.*, 2017, **8**, 1194.

70 G. Henkelman and H. Jónsson, *J. Chem. Phys.*, 2000, **113**, 9978–9985.

71 G. Henkelman, B. P. Uberuaga and H. Jónsson, *J. Chem. Phys.*, 2000, **113**, 9901–9904.